Research Article | 🔓 **Full Access**

Surface Functional Modification for Boosting Power Density of Hydrovoltaic Devices

Yanhui Liu, Zihao Li, Liying Wang, ✉, Xijia Yang, Yue Yang, Xuesong Li, Yi Jiang, Yang Gao, Wei Lü ✉

Abstract

Generating electricity based on the interaction between water and materials is a new green energy harvesting technology. However, the performance based on streaming potential generation is not sufficient to drive microelectronic devices with high power supply demands. In this work, an asymmetric sandwich structure is designed with adjustable performance of hydrovoltaic devices as a power system for micro-electronic devices. The flexible hydrovoltaic device structure that only consumes renewable energy is low-cost, non-polluting, and highly sustainable, achieving a satisfied output power density exceeding 124.5 $\mu W\cdot cm^{-2}$ (2075 $\mu W\cdot cm^{-3}$). Both experimental results and theoretical calculations reveal that the working principle of the device depends on the evaporation potential rather than the streaming potential. In addition, the integration of multiple devices makes it easy to drive electronic devices for correct operation and energy storage. For the first time, this integrated hydroelectric photovoltaic device has demonstrated the ability to charge commercial button-type lithium batteries with great success. The current work combines asymmetric structure and tunable performance, providing an alternative method for high-efficiency hydrovoltaic devices with high power density.

1 Introduction

The excessive consumption of non-renewable resources and the increasingly prominent ecological and environmental issues have made sustainable development the topic of contemporary environmental protection.[1, 2] As it is well known, water is not only the

essence of life but also the most abundant energy carrier on our planet. Water accounts for 71% of the Earth's surface and absorbs 35% of its solar energy, thus harboring a significant amount of energy.[3] Georg Quincke discovered that the interaction between water and solid materials can generate electrical energy. During this process, water flows through narrow channels under pressure gradients, generating electricity, which is termed the streaming potential.[4] This process is based on electrokinetic theory. Since its discovery, this phenomenon has sparked significant interest in the use of solid materials to obtain water energy.[5-9]

Hydrovoltaic devices are recognized as one of the prospective exemplars in various green energy collection systems. In recent years, many researchers have been committed to the preparation and function mechanisms of materials for hydrovoltaic devices.[10-14] Water that flows,[15, 16] fluctuates,[17] drips,[18] and evaporates directly interacts with carbon material,[19, 20] leading to electricity generation. This phenomenon generates a new energy conversion effect within the material, which we call the "hydrovoltaic effect". Subsequently, various hydrovoltaic materials represented by carbon nanotubes (CNTs) and graphene oxide (GO) have been continuously explored. In 2017, Guo et al. reported for the first time on the generation of electricity through natural evaporation of porous carbon black materials.[21] Due to the inherent property of all atoms on the exposed surface of carbon nanomaterials, they exhibit significant sensitivity to external stimuli and promote substantial interactions with water through electronic coupling. Zhou et al. mentioned the use of molecules or polymers to regulate the surface functional groups of carbon nanoparticles.[22] Wu et al. mentioned a continuous gradient chemical reduction strategy of graphene oxide for efficient evaporative power generation.[23] Despite significant advances in carbon-based nanomaterials, understanding reliable operating mechanisms and the output capabilities required for practical applications remains a challenge at present.

Hydroelectricity generation is mostly considered to be dominated by streaming potential.[24, 25] At present, due to limitations in existing technology, the physical behaviors of interactions between solids and liquids is unable to be effectively observed. A recent report by Guo et al. further pointed out that the generation of electricity by ethanol evaporation is independent of the streaming potential.[26] This evaporation behavior at the interface is known as the evaporative potential. Although theoretical simulations and experimental data do confirm the presence of evaporation potential, symmetric carbon electrodes still face challenges in effective charge collection.[27] Therefore, achieving higher power output is crucial for commercial applications.

In the present work, we designed an asymmetric sandwich structure hydrovoltaic device with capacitive characteristics. The upper electrode is made up of carbon cloth (CC) coated with carbon nanotubes (CNTs), and the bottom electrode is composed of an aluminum plate (Al) separated by porous filter paper (Figure S1, Supporting Information). Experimental results and model calculations confirm that the device operates based on evaporation potential rather than streaming potential, and can generate a voltage output of up to 0.71 V

and a current density (J) of 700 μA·cm^{-2}. The free electrons generated are efficiently used to produce a power density of 124.5 μW·cm^{-2} (2075 μW·cm^{-3}). This energy harvesting device is highly sustainable and environmentally friendly. Just two units are sufficient to power a calculator. The performance of the device can be easily scaled up, and the generated electricity can be stored in batteries and capacitors for later use.

2 Results and Discussion

2.1 Fabrication and Output Performance of Hydrovoltaic Devices

Figure 1a shows the preparation and assembling process of carbon nanotube-based hydrovoltaic devices, which are named CNTs/CB/PVDF@CC//Al (Carbon black and Poly vinylidene fluoride, CB and PVDF). The two electrodes are separated by a porous filter paper (Figure S2, Supporting Information) with an effective area of 1 cm^2. The SEM images of the four top electrodes are shown in Figure S3, Supporting Information. CC has a smooth surface. The smooth CC surface of PVDF@CC is covered with PVDF. The PVDF surface has CB particles in CB-PVDF@CC. It can be seen in CNTs/CB/PVDF@CC, CB particles are dotted on the surface of CNTs with cross-linked network structures, thus increasing the surface area of the CC. The CNTs/CB/PVDF@CC as the top electrode was used for characterization, and its XRD pattern exhibited characteristic peaks of carbon (Figure S4a, Supporting Information). Figure S4b, Supporting Information shows the contact angle comparison before and after plasma treatment of CNTs/CB/PVDF@CC. After plasma treatment, the electrode exhibits strong hydrophilicity, which is attributed to the presence of varying amounts of oxygen-containing functional groups in the carbon material. Therefore, UV-treated electrodes are used for characterization and performance testing of different electrodes.
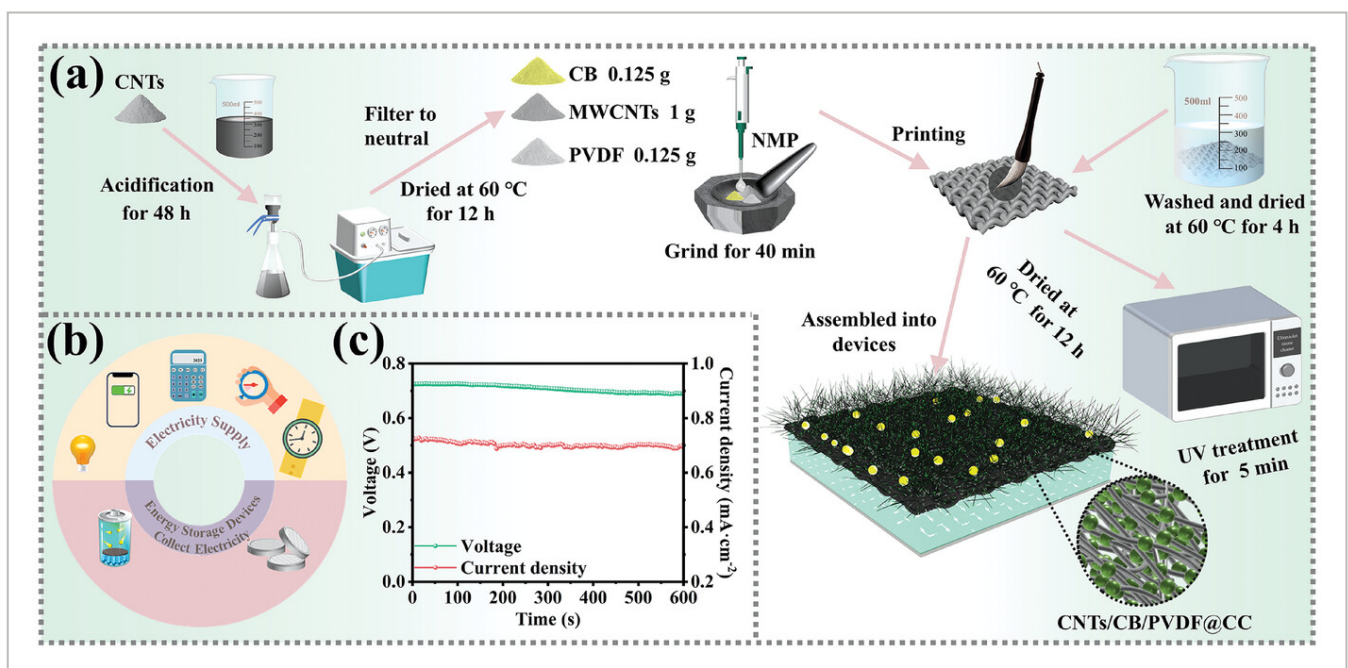

Figure 1

Open in figure viewer | ⬇**PowerPoint**

a) Preparation process of hydrovoltaic devices. b) The power generated by the device can either be utilized directly or stored for later use. c) Output performance of the CNTs/CB/PVDF@CC//Al device.

The quantity of functional groups directly affects the interaction between water and carbon nanomaterials. The XPS patterns in Figure S4c,d, Supporting Information reveal the presence of oxygen-containing functional groups. High-resolution Raman images and Raman spectra of CC are shown in Figure S4e,f, Supporting Information. The Raman spectrum demonstrates that CNTs/CB/PVDF@CC possesses a graphitic structure resembling amorphous carbon. The integration of multiple devices can either directly supply power to the microelectronic device or utilize energy storage components to accumulate the power generated in Figure 1b. The hydrovoltaic device CNTs/CB/PVDF@CC//Al can generate a voltage of 710 mV, and a current density of 700 µA·cm^{-2} as shown in Figure 1c.

2.2 Exploration of the Working Mechanism of the Hydrovoltaic Devices

Figure 2a illustrates the average voltage and current output of four different devices. Each type of device was measured with 10 devices to obtain the statistical average values. Figure 2b,c shows the error ranges for the voltage and current of 10 CNTs/CB/PVDF@CC//Al devices. The average performance output distribution of the other three types of devices is shown in Figure S5, Supporting Information. The voltage outputs of the four devices are all maintained between 0.7 and 0.8 V (Video S1, Supporting Information), while the current outputs are differentiated and their current density outputs are compared as J(CNTs/CB/PVDF@CC//Al) > J(CC//Al) > J(CB/PVDF@CC//Al) > J(PVDF@CC//Al) (Video S2, Supporting Information). Thus, the device of CNTs/CB/PVDF@CC//Al is used for later discussion without special mention. Figure S6, Supporting Information displays the performance output of the CNTs/CB/PVDF@CC//Al device within 2 h. The device exhibits good cyclic stability after long-term cycling, indicating its reusability.
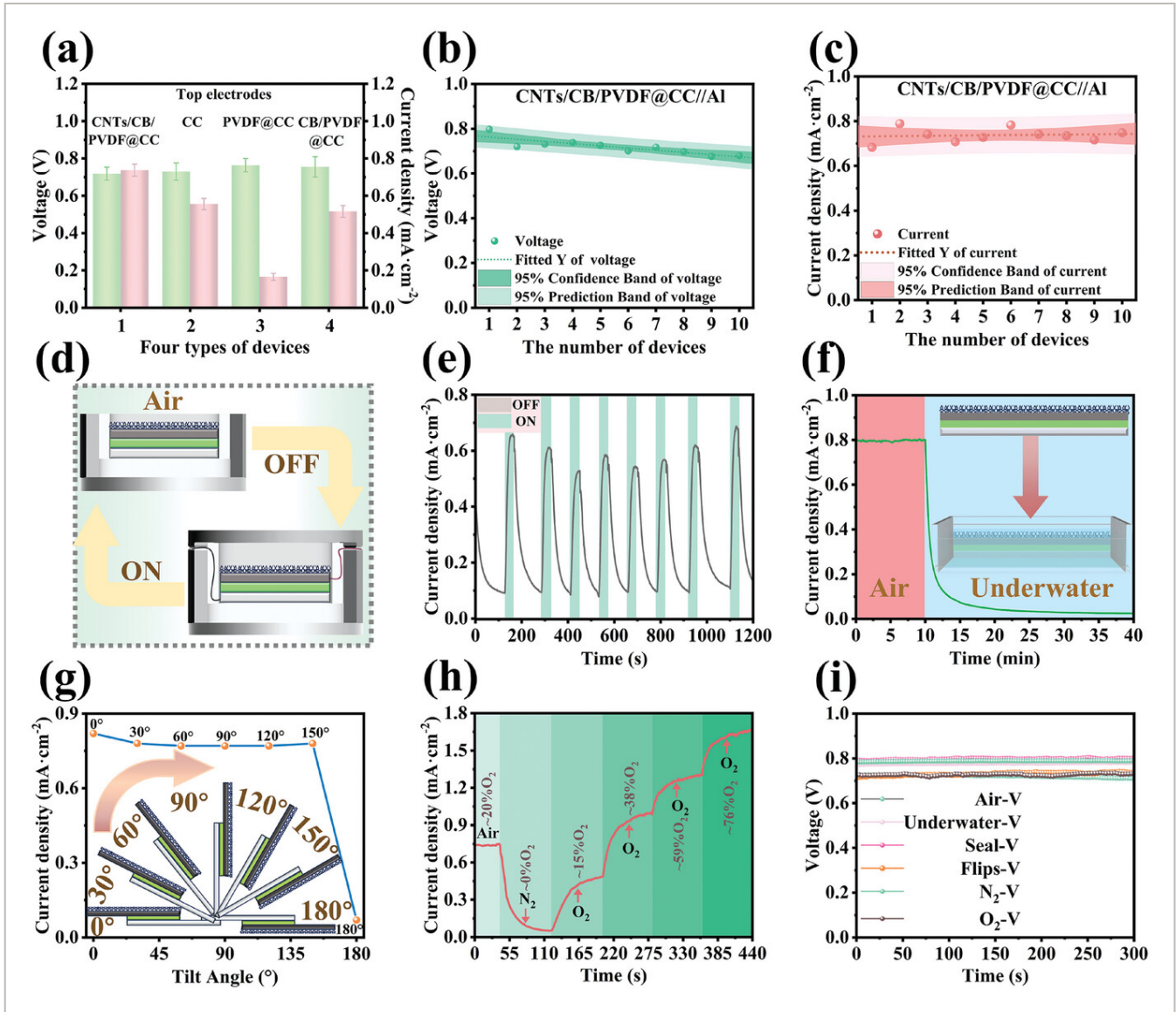
Figure 2

Open in figure viewer | ⬇PowerPoint

a) Average performance output of four types of devices. b) Voltage error bands for 10 devices. c) Current density error bands for 10 devices. d) Schematic diagram of sealing and opening of the device. The "ON" denotes air exposure, while the "OFF" signifies being sealed in the container. e) The device's J–t curve with intermittent air exposure. f) Current density values of devices exposed to air and immersed in water. g) The influence of the tilt angle on the current density. h) Current density of the device at different oxygen concentrations. i) Voltage values of the device under different conditions.

Figure **2d** shows the schematic diagram of the device intermittently exposed to air. When the device is sealed, the current of the hydrovoltaic electricity generator rapidly decreases, but it recovers after being exposed to air (Figure **2e**). The J–t curve of the hydrovoltaic electricity generator shows periodic variations, indicating that the current of the hydrovoltaic electricity generator is affected by water evaporation.[28-30] In order to quantitatively explain this evaporation behavior, we try to establish a quantitative evaporation testing platform to

conduct a quantitative analysis of the evaporation behavior (Figure S7, Supporting Information). Figure 2f shows the alteration in current when the device is immersed in water. In air, the current maintains a stable state. However, after immersion in water, the current gradually decreases due to obstruction of device evaporation.[31] Underwater, the device's current output can continue for an additional 10 min, a phenomenon we refer to as the "residual effect of evaporation" (Figure S8, Supporting Information). We observed that the current density value remains nearly constant for tilt angles less than 180° (Figure 2g). However, when the flip angle reaches 180°, the current density of the device experiences a significant decrease, which can be attributed to the decreased rate of evaporation. During the flip of the device, water may flow, but the current remains constant, indicating that the evaporation of the device is not influenced by the streaming potential. Furthermore, Figure 2h depicts the impact of gas environments and oxygen concentrations on the performance of the device. The setup of the gas environment is illustrated in Figure S9, Supporting Information. Obviously, the current density increases in air and decreases in N_2, indicating that oxygen is essential to achieve a high current output. The lower current output of PVDF@CC//Al could potentially be attributed to the fact that the PVDF covering hinders water evaporation from the surface, as well as limits its exposure to oxygen. The voltages measured under each of the aforementioned conditions do not show significant variations (Figure 2i). Figure S10, Supporting Information shows that voltage and current exhibit a stable behavior when the septum is present. However, when filter paper is not used as the septum, the voltage and current are measured at 50 mV and 190 μA, respectively (Red represents the absence of the septum, while green represents the presence of the septum). This indicates that the voltage generated by the device originates from the potential difference between the Al plate and the carbon materials. The current decreases without the diaphragm, which can be attributed to the reduced potential difference that hinders the efficient movement of the carriers.[32]

Figure 3a shows solar evaporation experiments are performed under 1 sun illumination. Figure 3b demonstrates the variation of the evaporation current with surface temperature for CNTs/CB/PVDF@CC and CC. It can be seen that the evaporation current rises as the surface temperature increases. In addition, the evaporation current of CNTs/CB/PVDF@CC is higher than that of CC, indicating that the interaction between CNTs/CB/PVDF@CC and water is stronger than that of CC. Further research is carried out to examine the impact of the evaporative environment on the generation of current at the CNTs/CB/PVDF@CC surface, as shown in Figure 3c i–vi. It could be concluded from schematics i, iv, and v that dry CNTs/CB/PVDF@CC, submerged CNTs/CB/PVDF@CC, and heated dry CNTs/CB/PVDF@CC do not generate current. This not only excludes the interference of thermoelectric effects,[33, 34] but also demonstrates that the interaction of water with the carbon material and the evaporation of water from the surface of the carbon material are essential for the generation of current. On the contrary, as shown in ii, iii, and vi, as the surface temperature of the carbon materials increases, the evaporation of water from their surface accelerates, leading to higher current. CNTs/CB/PVDF@CC generates a higher current than CC under

identical conditions (Table S1, Supporting Information). Therefore, the increase in the CB/PVDF@CC//Al current indicates that the addition of carbon material enhances the evaporation rate. Various bottom electrodes have achieved current and voltage output, in which Al and Sn have the best performance as shown in Figure 3d. This is because Al and Sn are non-inert electrodes with a large potential difference when in contact with carbon nanomaterials.[35] The intrinsic potential difference between two electrodes causes the steady voltage output. However, current output may depend on the migration of carriers formed during the water evaporation process. Mo, St, Cu, and Ti exhibit lower reactivity compared to Al and Sn. As a result, the potential difference between the asymmetric electrodes is relatively small, leading to insufficient carrier transmission power between the two electrodes and a decrease in the current output of the hydrovoltaic electricity generator. The use of inert bottom electrodes, such as Pt and Ag, as bottom electrodes also results in a weaker electrical output, indicating the presence of evaporation potential in devices consisting of a top carbon material electrode and bottom electrode material. Figure 3e shows that the CV curves exhibit a symmetrical shape, and no discernible redox peaks are observed at different scan rates.[36, 37] Figure 3f shows the current output when simulating an Al-air battery (**Figure 4a**).[38] According to reports, when the negative electrode (active bottom electrode) of the device is immersed in water, electrons inside the device flow from the negative electrode to the positive electrode (inert top electrodes and carbon electrodes), forming an air battery and generating high current.[39] However, in this article, the current when using inert top electrodes can be ignored, and large currents can only be generated when using carbon electrodes. This not only precludes the influence of air batteries on the current but also demonstrates that the coupling of water to carbon material is key to the generation of electrical energy from evaporation.
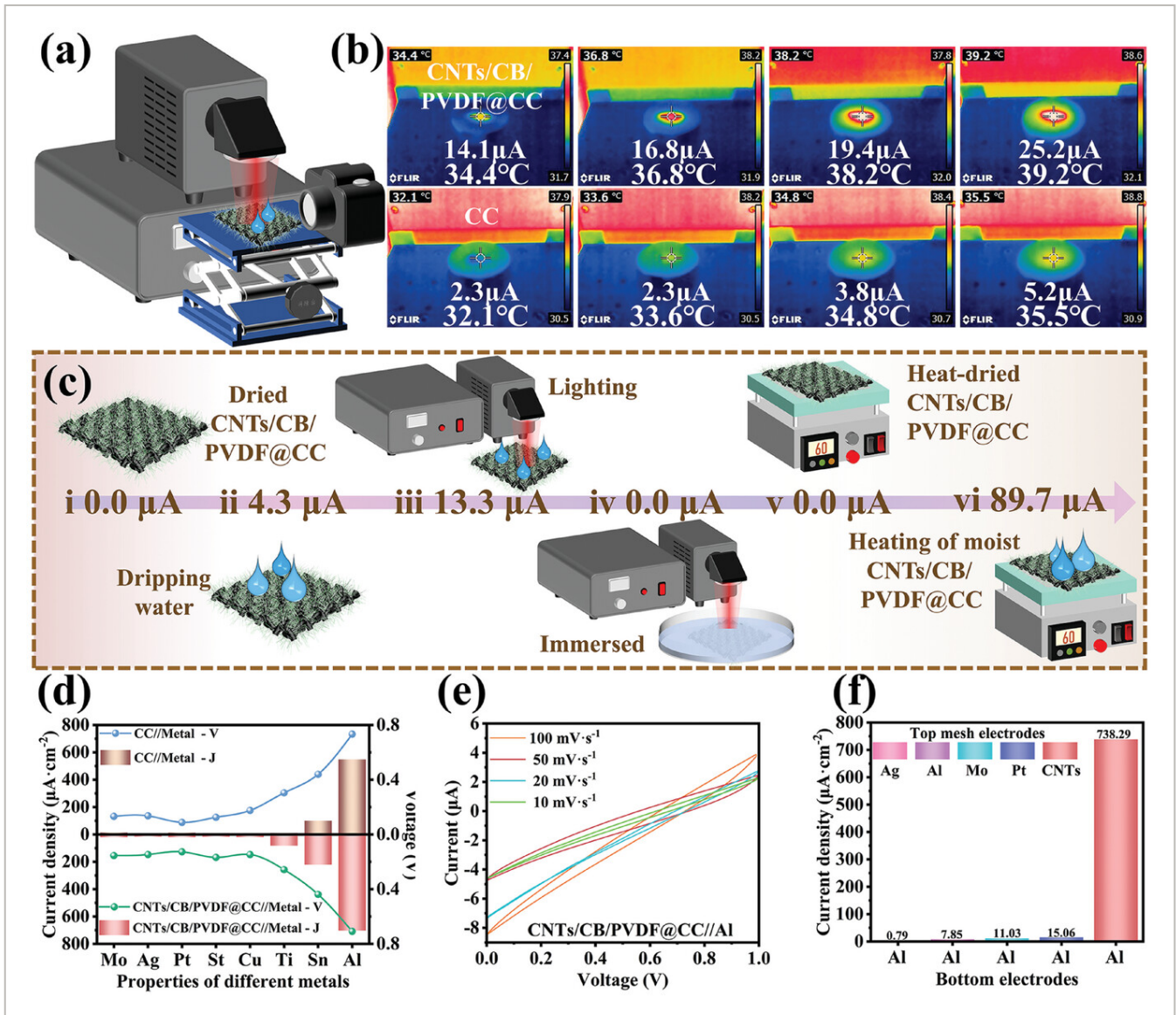
Figure 3

Open in figure viewer | PowerPoint

a) Schematic diagrams of the top electrode tested under the sunlight simulator ($1 Kw \cdot m^{-2}$). b) Temperature and current variation of the top electrode in air under 1 sun illumination. c) Current output of CNTs/CB/PVDF@CC measured under different conditions. i) Dried CNTs/CB/PVDF@CC, ii) wetted CNTs/CB/PVDF@CC, iii) wetted CNTs-CB-PVDF@CC and light illumination, iv) immersed CNTs/CB/PVDF@CC and light illumination, v) dried CNTs/CB/PVDF@CC and heated by heating platform, and vi) wetted CNTs/CB//PVDF@CC and heated by heating platform. d) The output performance of the two top electrodes of CC and CNTs/CB/PVDF@CC achieved with different bottom electrodes. e) The CV curves of the device. f) The impact of different top mesh electrodes on water evaporation.
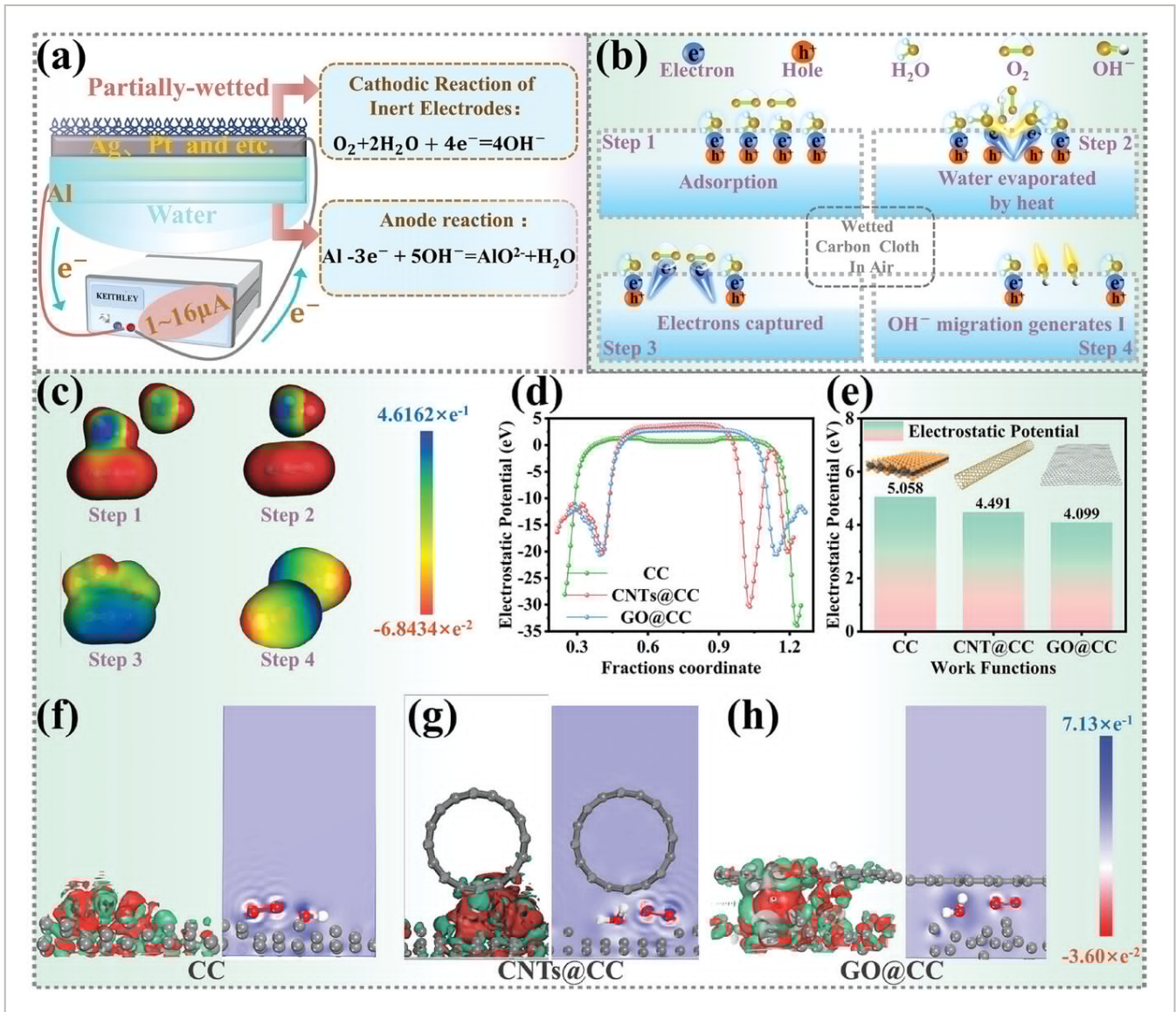
Figure 4

a) Schematic diagram for verifying the presence of Al-Air batteries. b) Schematic illustration of the working mechanism. c) Simulation diagram of the evaporation mechanism. d) Substance work function potential diagram. e) Working function for amorphous carbon (CC), carbon nanotubes (CNTs), and graphene oxide (GO). f–h) are the molecular models and differential charge density for CC, CNTs, and GO, respectively.

2.3 Molecular Simulations of Device Operating Mechanisms by DFT and MD

The working mechanism of the device can be explained as the interaction between water and carbon material, leading to the hybridization of the S and P orbitals and forming a loose electron cloud.[40] During the process of water evaporation, the electron cloud is pulled to the top carbon electrodes' surface by H_2O molecules and is rapidly trapped by oxygen to produce OH^- ions, which move rapidly under potential difference to generate a high current

output. Figure 4b,c show the evaporation process. In step 1, H_2O molecules and O_2 are adsorbed on the top carbon electrodes' surface. The interaction between H_2O molecules and carbon materials causes the hybridization of the S orbitals and the P orbitals, leading to the formation of a loose electron cloud at the carbon-based materials' surface. The water molecules absorb heat energy from the surroundings to vaporize from the surface of carbon nanomaterials (step 2). Simultaneously, as H_2O molecules evaporate, the loose electron clouds are drawn to the surface of carbon-based materials. The evaporation of water molecules draws free electrons to the carbon-based materials' surface, where they are rapidly captured by oxygen molecules (step 3) and then generated into OH^- (step 4), which moves under the action of the potential difference to produce current. Molecular dynamics simulations and density functional theory (DFT) calculations offer a more intuitive explanation of the water evaporation mechanism. Figure S11, Supporting Information illustrates the evaporation process of H_2O molecules at the carbon nanotube materials' surface calculated using molecular dynamics. At room temperature, water molecules slowly evaporate off the surface of carbon-based materials and transform into water vapor over time. Figure 4d,e shows the work function of amorphous carbon cloth (CC), carbon nanotubes (CNTs), and graphene oxide (GO). >0 indicates that coating the CC surface with CNT or GO reduces the energy for electrons to escape from the material's interior. The simulation results serve as a theoretical foundation for the higher evaporation current in CNTs/CB/PVDF@CC compared to that of CC. The blue color indicates high electron density, while the red color represents low electron density. Figure 4f–h represents the differential charge densities of the three carbon materials, respectively. These visualized images show the process of oxygen capturing electrons during the evaporation of water molecules.

Figure 5a–c demonstrates the low surface charge density of carbon material in the absence of water and oxygen. However, the presence of water evaporation and oxygen significantly enhances the surface charge density. Figure 5d–f displays the density of states for the dry carbon materials. These results further indicate that the energy threshold required for electrons to escape from the interior of CNTs and GO is lower than that of CC. According to Figure 5g–i, the evaporation of water on the surface of the carbon material induces hybridization of the S and P orbitals within the carbon material, resulting in the formation of stacked electron cloud arrangements on the surface of the carbon-based materials. From Figure 5d–i, it is evident that the surface of wet carbon materials has a higher density of free electrons compared to dry carbon materials. Additionally, Figure S12, Supporting Information illustrates the statistical average values of DOS for different carbon materials under wet and dry conditions. In summary, first-principles calculations and molecular dynamics simulations indicate that oxygen molecules capture some electrons through the evaporation process of water, leading to the formation of OH^-. OH^- moves with the help of the potential difference to generate current output. To validate this working mechanism, the variations in surface temperature and pH values of carbon materials in the device are monitored using an infrared camera and pH meter as shown in Figure S13, Supporting Information. As the surface temperature of the carbon material increases, evaporation will

be accelerated accordingly, and there will be a noticeable shift in the pH of the carbon material surface, consistent with the hypothesis proposed by the simulation calculations. The production of OH^- groups is positively correlated with temperature. As the temperature rises, the rate of water evaporation accelerates, leading to a greater production of OH^- groups.
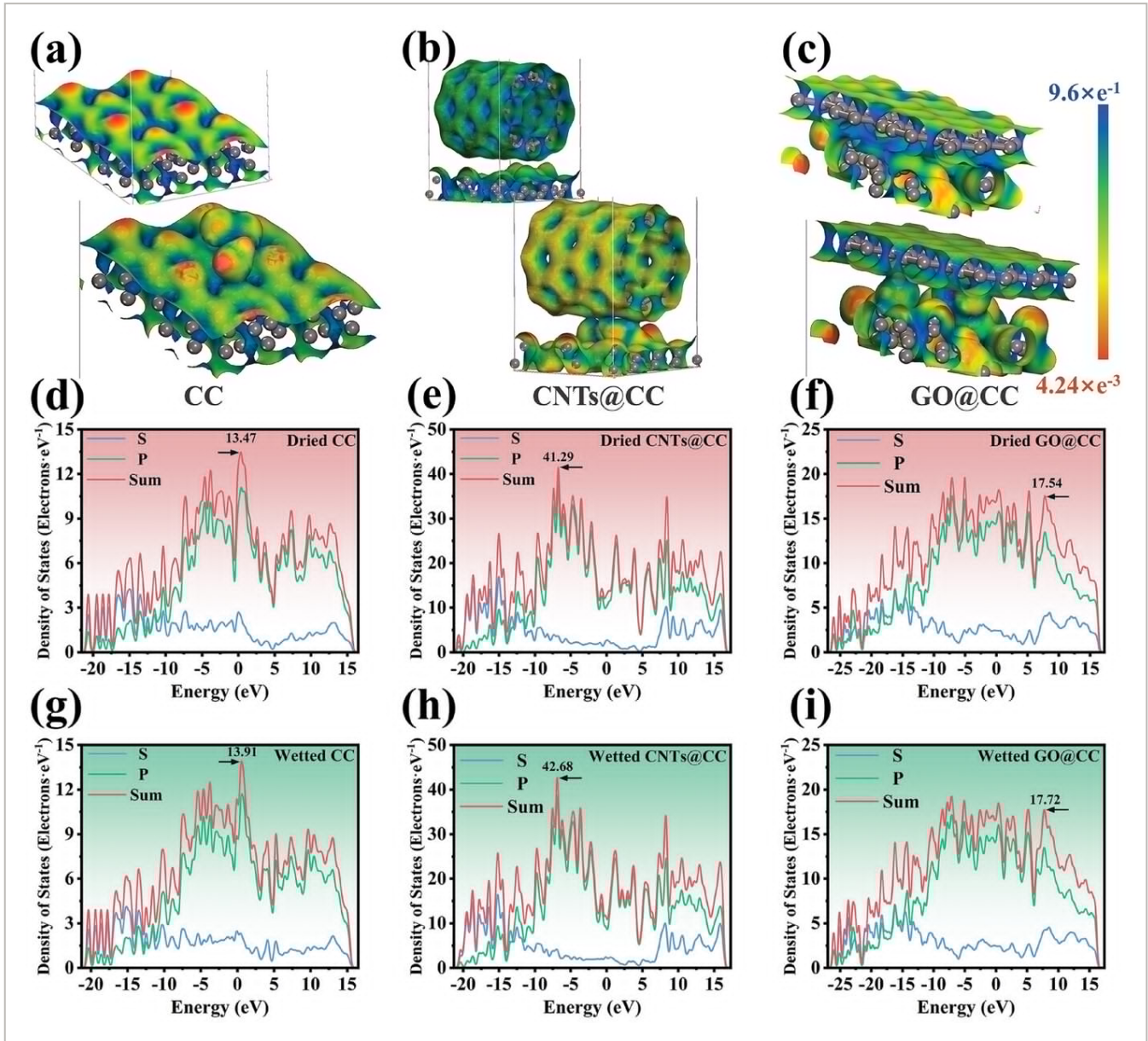

Figure 5

Open in figure viewer | **⬇PowerPoint**

a–c) are the impact of changing environmental conditions on the localized electron density at the carbon surface. d–f) are the density of states of dried carbon materials. g–i) are the density of states of wetted carbon materials.

2.4 Impact of Various Factors on the Output Performance of Devices

As the temperature increases, the evaporation rate on the top carbon electrode[41, 42] leads to the current output increases, as shown in **Figure 6a**. The evaporation currents of the device at 34 and 90 °C are represented as and , respectively. The temperature is raised from 34 to 90 °C, and the current output of the device changes by ≈ 0.75 mA, which is known as .
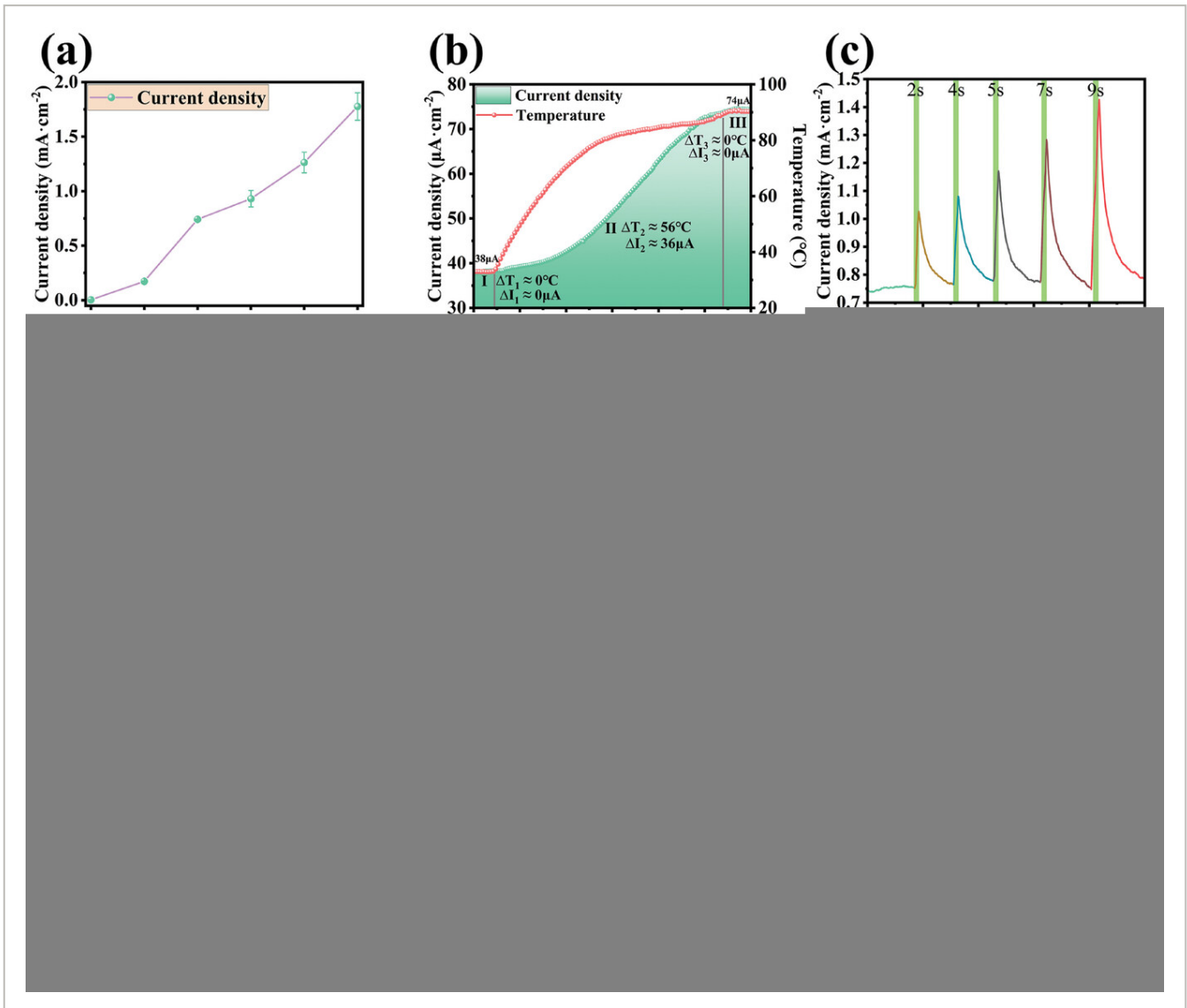

Figure 6

Open in figure viewer | ⬇**PowerPoint**

a) The effect of temperature on device current output. b) Corrosion current of the device in the nonevaporated state. c) *J*–*t* curve for different heating times. d) *J*–*t* curve for changes in humidity. e) The *J*–*t* curve after changing the wind speed at the electrode surface. f,g) Output of devices with different layers of diaphragm. h,i) Voltage and current densities achieved with different areas of overlap between the two electrodes.

The corrosion of the active electrode contributes to the current output too. Figure S14, Supporting Information and Figure 6b show a schematic for inhibiting hydrovoltaic electricity generator evaporation and the current curve of the hydrovoltaic electricity generator in the nonevaporated state, respectively. At room temperature (stage I), the corrosion current of

the device without evaporation was 38 µA, which is labeled as , However, when the temperature is raised to 90 °C (stage III), the current of the hydrovoltaic electricity generator increases to 74 µA, which is labeled as , and the current of the hydrovoltaic electricity generator changed by only 36 µA, which is known as (stage II). The results of demonstrate that the increased current output is mainly attributed to water evaporation as the temperature increases. To simulate the corrosion current output of the device under evaporation conditions, the device is sealed in a weak alkaline solution (pH = 8) to prevent water evaporation. In this case, the device's current output represents the corrosion current. Figure S15, Supporting Information shows the corrosion current curve of the device. At this point, the device's corrosion current is 66 µA, which is marked as $I^{Corrosion}$ = 66 µA. However, the average current generated by 10 devices under evaporation is 737 µA, which is marked as I^{Total} = 737 µA. Therefore, the corrosion-generated current accounts for only 8.9% of the total current output of the device, indicating a relatively low contribution of corrosion to the device's output performance. During normal operation of the equipment, the current curve after changing the heating time is shown in Figure 6c. The high evaporation rate results in higher current output. Figure 6d shows the relationship between humidity and current output at room temperature. The current output of the device decreases as humidity increases, indicating that higher humidity hinders water evaporation.[43] The current does not decrease to zero here because the device may still exhibit evaporation behavior at 29 °C. The device's weak corrosion current also contributes to this portion of the current. The current output of the device is affected by changing wind speed as shown in Figure 6e. The current output remains unchanged for the normal operation of the device. However, as the wind speed on the surface of the device increases, the current output increases, indicating that the higher wind speed enhances water evaporation.[44-46] The primary factors influencing the device's operation are oxygen concentration, temperature, humidity, and wind speed. Higher oxygen concentration, elevated temperature, reduced humidity, and increased wind speed all serve to enhance the device's working mechanism and improve the power density output (Figure S16, Supporting Information). Figure 6f,g shows the impact of the number of diaphragm layers on the voltage and current density of the device. The voltage is determined by the potential difference between the top and bottom electrodes. However, as the number of filter papers increases, the current output decreases.[47] This is because a thicker diaphragm layer resulted in insufficient ion transport dynamics, thus hindering efficient charge collection by the electrodes. When the length remains constant and the width increases, the output of voltage and current can be observed in Figure 6h,i. There is no significant change in voltage. However, with an increase in width, the current also increases,[9, 48-51] which adheres to the circuit series and parallel criteria. Therefore, expanding the overlap area proves to be an effective method for increasing power output.

2.5 Power Density Testing of Hydrovoltaic Devices and Its Applications

Figure 7a shows the voltage and current output of CNTs/CB/PVDF@CC//Al with different loading resistances. As the load resistance increases, the voltage increases, while the current density decreases. The peak output power density of the device is 124.5 µW·cm^{-2} at a load resistance of 400 Ω as shown in Figure 7b. The device CNTs/CB/PVDF@CC//Al has a much higher power density than that of CC//Al (Figure S17, Supporting Information), indicating that the surface functional modification of the CC helps to enhance the evaporation rate, thus increasing the power density. The devices in this paper achieve the best record compared to previous work as shown in Figure 7c,d.
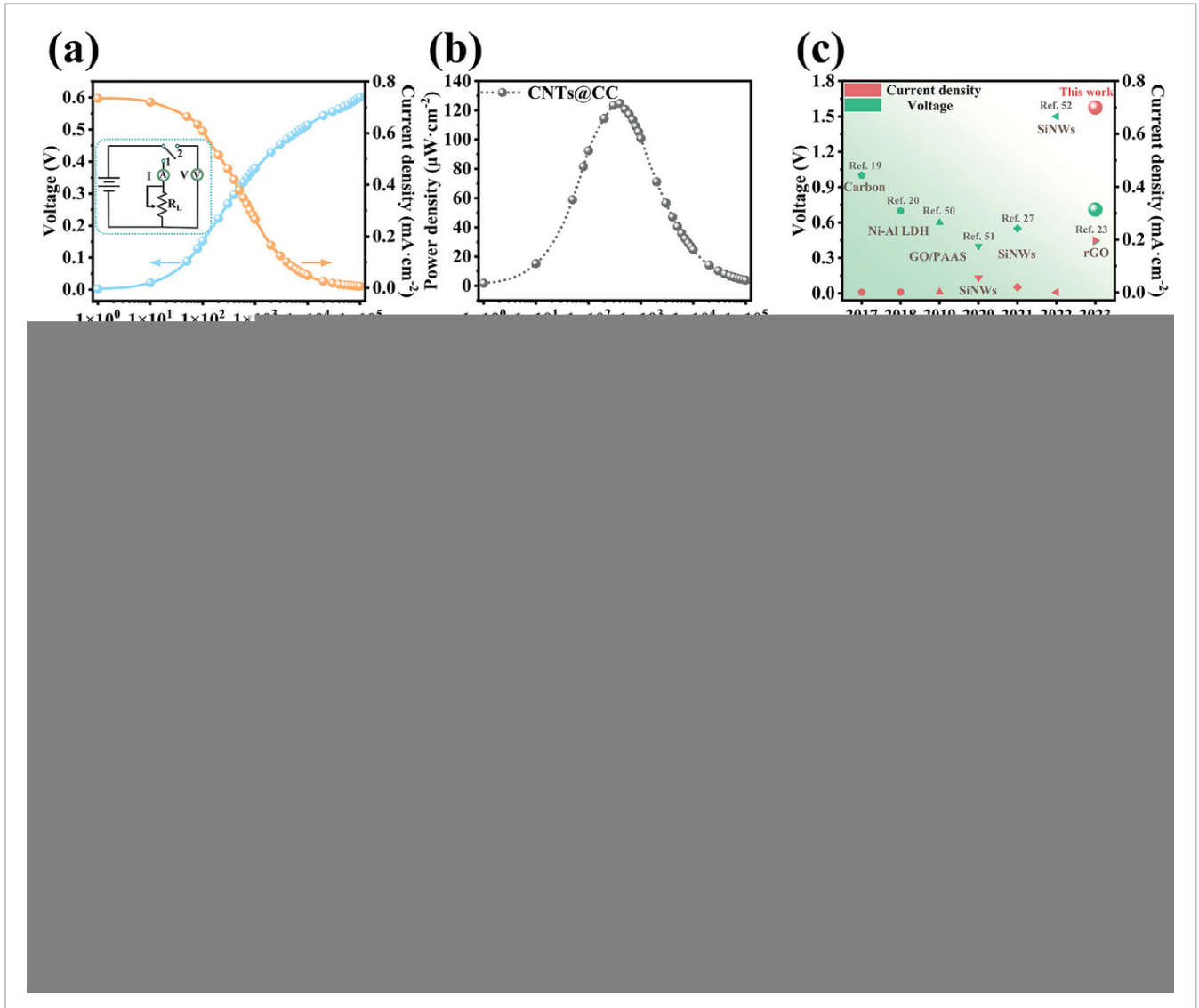

Figure 7

Open in figure viewer | ⬇PowerPoint

a) Output performance of the device at different loads. b) The power density of the device at different loads. c) Comparison of voltage and current density of the present work with previous reports. d) Comparison of the power density of the present work with previous reports. e) Voltage output signals for 1–10 device units in series. f) Current output signals for 1–10 device units in parallel. g) *V–t* curve for charging batteries by hydrovoltaic devices. h) *V–t* curve

for charging capacitors of different capacities by hydrovoltaic devices. i) The output voltage curve is amplified by an amplifier circuit and two devices in series to drive the calculator.

Voltage output can be increased by connecting device units in series. A voltage of 0.7 V is generated by one device unit, and a 6.5 V output can be obtained by connecting 10 device units in series as shown in Figure 7e. As shown in Figure S18a, Supporting Information, the voltage output shows a good linear relationship with the number of devices, demonstrating an excellent scalability of the device. Furthermore, the current output of hydrovoltaic devices can be easily boosted to 6.9 mA by integrating 10 units in parallel as shown in Figure 7f. The current output shows a good linear relationship with the number of device units (Figure S18b, Supporting Information). Figure 7g shows that a device with a 2 × 2 series-parallel connection can charge directly for a battery from 0.9 to 1.4 V without the need for an external rectifier circuit. This paper presents, for the first time, that aqueous hydrovoltaic devices can charge for commercial button-type lithium batteries (LIR2016), indicating that electricity generated through evaporation can be continuously stored in an energy storage element for future backup. A device unit charges capacitors with different capacities, as shown in Figure 7h. Two devices in the series generate enough power to drive the calculator (Figure 7i and Video S3, Supporting Information). Figure 7i and Figure S19, Supporting Information show the voltage of eight devices in series amplified to 40 V by an amplifier circuit. The utilization of amplification circuits not only reduces the size of the integrated device but also allows the voltage to be easily modulated to the desired value.

3 Conclusion

In summary, we have successfully prepared a sandwich structure hydraulic voltage device with asymmetric electrodes. Plasma-treated CNTs/CB/PVDF@CC exhibit not only strong hydrophilicity and enhanced interaction with water but also increased electrode surface area and improved the evaporation rate of the device. The solar-driven evaporation experiment demonstrated that increasing the interface surface area of the electrodes contributes to enhancing the evaporative performance at the interface. A unit with an area of only 1 cm^2 (0.06 cm^3) produces a power density of 124.5 $\mu W \cdot cm^{-2}$ (2075 $\mu W \cdot cm^{-3}$). Experimental results and theoretical calculations confirm that the device operates based on the evaporation potential within pure-water systems, generated by amorphous carbon and carbon nanotube coupling with water to produce free electrons. Present aqueous hydrovoltaic devices can charge for commercial button-type lithium batteries, and two-unit devices in series connection can power a calculator. The performance can be easily scaled up for greater electrical energy generation. The generated electricity can be conveniently stored for backup and future use. This environmentally friendly device provides sustainable and efficient energy.

4 Experimental Section

Fabrication Process of Devices

Experimental reagents, pretreatment methods, and material characterization can be found in the Supporting Information. The Al plate (2 × 1 cm) was ultrasonically cleaned in alcohol, acetone, and deionized water for 15 min, and dried at 60 °C for 5 min. The top electrode was prepared by mixing the active materials of multi-walled carbon nanotubes (MWCNTs), conductive carbon black (CB), and poly(vinylidene fluoride) (PVDF) binders in a weight ratio of 8:1:1 in 1-methyl-2-pyrrolidinone (NMP), which was further coated on CC by brush and dried overnight at 60 °C in vacuum. Before assembling, the top electrode was treated in a UV-ozone cleaner for 5 min. The device with CNTs/CB/PVDF@CC as the top electrode and Al as the bottom electrode was labeled as CNTs/CB/PVDF@CC//Al, which was separated with filter paper. Similarly, the devices formed by UV-treated CC and Al were called CC//Al. The devices formed by PVDF-loaded CC and Al were called PVDF@CC//Al. The devices formed by coating the surface of CC with a composite material of PVDF and CB (PVDF/CB = 1/1, m/m), along with Al, were referred to as CB/PVDF@CC//Al.

Simulation of Computational Methods

The first-principle calculation was performed. The truncation energy of 400 eV was adopted for wave function expansion. The energy converged to 10^{-5} eV, achieving high accuracy. Brillouin zone integration used a 2 × 2 × 1 k-grid for calculating the density of states. To prevent interaction, a vacuum layer with a thickness of 14 Å was introduced. The calculation of the differential charge density was carried out using the Castep module. The Forcite module calculated and analyzed the molecular dynamics of water evaporation from the surfaces of CNTs.

Acknowledgements

Conflict of Interest

The authors declare no conflict of interest.

Open Research

Data Availability Statement

The data that support the findings of this study are available from the corresponding author upon reasonable request.

Supporting Information

Filename	Description
adfm202312666-sup-0001-SuppMat.pdf 1.8 MB	Supporting Information
adfm202312666-sup-0002-VideoS1.mp4 3.7 MB	Supplemental Movie 1
adfm202312666-sup-0003-VideoS2.mp4 6.4 MB	Supplemental Movie 1
adfm202312666-sup-0004-VideoS3.mp4 5.9 MB	Supplemental Movie 1

Please note: The publisher is not responsible for the content or functionality of any supporting information supplied by the authors. Any queries (other than missing content) should be directed to the corresponding author for the article.

References

1 R. Luque, L. Herrero-Davila, J. M. Campelo, J. H. Clark, J. M. Hidalgo, D. Luna, J. M. Marinas, A. A. Romero, *Energy Environ. Sci.* 2008, **1**, 542.

CAS | **Web of Science®** | **Google Scholar**

2 R. Eisenberg, *ACS Energy Lett.* 2018, **3**, 1521.

CAS | **Web of Science®** | **Google Scholar**

3 G. L. Stephens, J. Li, M. Wild, C. A. Clayson, N. Loeb, S. Kato, T. L'ecuyer, P. W. Stackhouse, M. Lebsock, T. Andrews, *Nat. Geosci.* 2012, **5**, 691.

CAS | **Web of Science®** | **Google Scholar**

4 S. Wall, *J. Colloid Interface Sci.* 2010, **15**, 119.

CAS | **Google Scholar**

5　T. Xu, X. Ding, C. Shao, L. Song, T. Lin, X. Gao, J. Xue, Z. Zhang, L. Qu, *Small* 2018, **14**, 1704473.

Web of Science® | **Google Scholar**

6　S. Chen, H. Xia, Q.-Q. Ni, *Adv. Electron. Mater.* 2021, **7**, 2100222.

CAS | **Web of Science®** | **Google Scholar**

7　F. Zhao, Y. Guo, X. Zhou, W. Shi, G. Yu, *Nat. Rev. Mater.* 2020, **5**, 388.

Web of Science® | **Google Scholar**

8　W. He, L. Zhou, M. Wang, Y. Cao, X. Chen, X. Hou, *Sci. Bull.* 2021, **66**, 1472.

CAS | **PubMed** | **Web of Science®** | **Google Scholar**

9　B. Shao, Y. Wu, Z. Song, H. Yang, X. Chen, Y. Zou, J. Zang, F. Yang, T. Song, Y. Wang, M. Shao, B. Sun, *Nano Energy* 2022, **94**, 106917.

CAS | **Web of Science®** | **Google Scholar**

10　W.-C. Lee, A. Ronghe, L. F. Villalobos, S. Huang, M. Dakhchoune, M. Mensi, K.-J. Hsu, K. G. Ayappa, K. V. Agrawal, *ACS Nano* 2022, **16**, 15382.

CAS | **PubMed** | **Web of Science®** | **Google Scholar**

11　Y. Wang, T. Guo, Z. Tian, K. Bibi, Y.-Z. Zhang, H. N. Alshareef, *Adv Mater* 2022, **34**, 2108560.

CAS | **Web of Science®** | **Google Scholar**

12　Y. Li, H. Chen, S. Xiao, M. A. Alibakhshi, C.-W. Lo, M.-C. Lu, C. Duan, *ACS Nano* 2019, **13**, 3363.

CAS | **PubMed** | **Web of Science®** | **Google Scholar**

13　K. H. Lee, D. J. Kang, W. Eom, H. Lee, T. H. Han, *Chem. Eng. J.* 2022, **430**, 132759.

CAS | **Web of Science®** | **Google Scholar**

14　J. You, J. Shao, Y. He, F. F. Yun, K. W. See, Z. L. Wang, X. Wang, *ACS Nano* 2021, **15**, 8706.

| **CAS** | **PubMed** | **Web of Science®** | **Google Scholar** |

---

15   P. Král, M. Shapiro, *Phys. Rev. Lett.* 2001, **86**, 131.

| **CAS** | **PubMed** | **Web of Science®** | **Google Scholar** |

---

16   H. Cheng, Y. Huang, F. Zhao, C. Yang, P. Zhang, L. Jiang, G. Shi, L. Qu, *Energy Environ. Sci.* 2018, **11**, 2839.

| **CAS** | **Web of Science®** | **Google Scholar** |

---

17   F. Huang, P. Yang, Z. Liu, D. Yang, L. Huang, Y. Shi, X. Tao, Y. Chen, H. Li, X. Chen, Z. Bian, *Nano Energy* 2023, **110**, 108346.

| **CAS** | **Google Scholar** |

---

18   X. Wang, S. Fang, J. Tan, T. Hu, W. Chu, J. Yin, J. Zhou, W. Guo, *Nano Energy* 2021, **80**, 105558.

| **CAS** | **Web of Science®** | **Google Scholar** |

---

19   T. Ding, K. Liu, J. Li, G. Xue, Q. Chen, L. Huang, B. Hu, J. Zhou, *Adv. Funct. Mater.* 2017, **27**, 1700551.

| **CAS** | **Web of Science®** | **Google Scholar** |

---

20   J. Sun, P. Li, J. Qu, X. Lu, Y. Xie, F. Gao, Y. Li, M. Gang, Q. Feng, H. Liang, X. Xia, C. Li, S. Xu, J. Bian, *Nano Energy* 2019, **57**, 269.

| **CAS** | **Web of Science®** | **Google Scholar** |

---

21   G. Xue, Y. Xu, T. Ding, J. Li, J. Yin, W. Fei, Y. Cao, J. Yu, L. Yuan, L. Gong, J. Chen, S. Deng, J. Zhou, W. Guo, *Nat. Nanotechnol.* 2017, **12**, 317.

| **CAS** | **PubMed** | **Web of Science®** | **Google Scholar** |

---

22   K. Liu, P. Yang, S. Li, J. Li, T. Ding, G. Xue, Q. Chen, G. Feng, J. Zhou, *Angew. Chem., Int. Ed.* 2016, **55**, 8003.

| **CAS** | **PubMed** | **Web of Science®** | **Google Scholar** |

23　Q. Liu, J. Liang, B. Tian, E. Xue, X. Zhang, P. Guo, K. Zheng, G. Tang, W. Wu, *Small Methods* 2023, **7**, 2300304.

CAS | **Web of Science®** | **Google Scholar**

24　S. Zhang, S. Fang, L. Li, W. Guo, *Sci. China Technol. Sci.* 2021, **64**, 629.

CAS | **Web of Science®** | **Google Scholar**

25　J. Bae, T. G. Yun, B. L. Suh, J. Kim, I.-D. Kim, *Energy Environ. Sci.* 2020, **13**, 527.

CAS | **Web of Science®** | **Google Scholar**

26　S. Fang, J. Li, Y. Xu, C. Shen, W. Guo, *Joule* 2022, **6**, 690.

Web of Science® | **Google Scholar**

27　B. Shao, Z. Song, X. Chen, Y. Wu, Y. Li, C. Song, F. Yang, T. Song, Y. Wang, S.-T. Lee, B. Sun, *ACS Nano* 2021, **15**, 7472.

CAS | **PubMed** | **Web of Science®** | **Google Scholar**

28　F. Yu, J. Li, Y. Jiang, L. Wang, X. Yang, Y. Yang, X. Li, K. Jiang, W. Lü, X. Sun, *Adv. Sci.* 2023, **10**, 2302941.

CAS | **Google Scholar**

29　J. H. Park, S. H. Park, J. Lee, S. J. Lee, *ACS Sustainable Chem. Eng.* 2021, **9**, 5027.

CAS | **Web of Science®** | **Google Scholar**

30　X. Liu, H. Gao, J. E. Ward, X. Liu, B. Yin, T. Fu, J. Chen, D. R. Lovley, J. Yao, *Nature* 2020, **578**, 550.

CAS | **PubMed** | **Web of Science®** | **Google Scholar**

31　K. Saha, J. Deka, K. Raidongia, *ACS Appl. Energy Mater.* 2021, **4**, 8410.

CAS | **Web of Science®** | **Google Scholar**

32　L. Li, S. Gao, M. Hao, X. Yang, S. Feng, L. Li, S. Wang, Z. Xiong, F. Sun, Y. Li, Y. Bai, Y. Zhao, Z. Wang, T. Zhang, *Nano Energy* 2021, **85**, 105970.

| **CAS** | **Web of Science®** | **Google Scholar** |

33   J. Li, F. Yu, Y. Jiang, L. Wang, X. Yang, X. Li, W. Lü, X. Sun, *Sol. RRL* 2022, **6**, 2101011.

| **CAS** | **Web of Science®** | **Google Scholar** |

34   M. Jiang, W. Zhang, S. An, Q. Shen, B. Fu, C. Song, P. Tao, J. Wang, W. Shang, T. Deng, *Nano Energy* 2023, **117**, 108916.

| **CAS** | **Google Scholar** |

35   T. Tabrizizadeh, Z. She, K. Stamplecoskie, G. Liu, *ACS Omega* 2022, **7**, 28275.

| **CAS** | **PubMed** | **Web of Science®** | **Google Scholar** |

36   P. Luan, N. Zhang, W. Zhou, Z. Niu, Q. Zhang, L. Cai, X. Zhang, F. Yang, Q. Fan, W. Zhou, Z. Xiao, X. Gu, H. Chen, K. Li, S. Xiao, Y. Wang, H. Liu, S. Xie, *Adv. Funct. Mater.* 2016, **26**, 8178.

| **CAS** | **Web of Science®** | **Google Scholar** |

37   K. Shi, X. Yang, E. D. Cranston, I. Zhitomirsky, *Adv. Funct. Mater.* 2016, **26**, 6437.

| **CAS** | **Web of Science®** | **Google Scholar** |

38   Y. Wang, W. Pan, K. W. Leong, S. Luo, X. Zhao, D. Y. C. Leung, *Green Energy Environ.* 2023, **8**, 1117.

| **CAS** | **Google Scholar** |

39   C. Zheng, S. Fang, W. Chu, J. Tan, B. Tian, X. Jiang, W. Guo, *Nano Res.* 2023, **16**, 11320.

| **CAS** | **Web of Science®** | **Google Scholar** |

40   M. Zhu, J. Li, X. Yang, X. Li, L. Wang, W. Lü, *Appl. Surf. Sci.* 2023, **624**, 157106.

| **CAS** | **Google Scholar** |

41   H. Jin, S. G. Yoon, W. H. Lee, Y. H. Cho, J. Han, J. Park, Y. S. Kim, *Energy Environ. Sci.* 2020, **13**, 3432.

| **CAS** | **Web of Science®** | **Google Scholar** |

42   M. Wu, M. Peng, Z. Liang, Y. Liu, B. Zhao, D. Li, Y. Wang, J. Zhang, Y. Sun, L. Jiang, *ACS Appl. Mater. Interfaces* 2021, **13**, 26989.

CAS │ **PubMed** │ **Web of Science®** │ **Google Scholar** │

43   H. He, T. Zhao, H. Guan, T. Zhong, H. Zeng, L. Xing, Y. Zhang, X. Xue, *Sci. Bull.* 2019, **64**, 1409.

CAS │ **PubMed** │ **Web of Science®** │ **Google Scholar** │

44   J. Garemark, F. Ram, L. Liu, I. Sapouna, M. F. Cortes Ruiz, P. T. Larsson, Y. Li, *Adv. Funct. Mater.* 2022, **33**, 2208933.

Web of Science® │ **Google Scholar** │

45   Z. Sun, C. Han, S. Gao, Z. Li, M. Jing, H. Yu, Z. Wang, *Nat. Commun.* 2022, **13**, 5077.

CAS │ **PubMed** │ **Google Scholar** │

46   Q. Wei, W. Ge, Z. Yuan, S. Wang, C. Lu, S. Feng, L. Zhao, Y. Liu, *Nano Res.* 2023, **16**, 7496.

Web of Science® │ **Google Scholar** │

47   K. Wang, W. Xu, J. Li, H. Zheng, S. Sun, W. Song, Y. Song, Z. Ding, R. Zhang, Y. Sun, H. Zhang, J. Li, Z. Wang, *Nano Energy* 2023, **111**, 108388.

CAS │ **Google Scholar** │

48   J. Park, S. Song, Y. Yang, S.-H. Kwon, E. Sim, Y. S. Kim, *J. Am. Chem. Soc.* 2017, **139**, 10968.

CAS │ **PubMed** │ **Web of Science®** │ **Google Scholar** │

49   Z. Li, X. Ma, D. Chen, X. Wan, X. Wang, Z. Fang, X. Peng, *Adv. Sci.* 2021, **8**, 202004552.

Google Scholar │

50   Y. Huang, H. Cheng, C. Yang, H. Yao, C. Li, L. Qu, *Energy Environ. Sci.* 2019, **12**, 1848.

CAS │ **Web of Science®** │ **Google Scholar** │

51   Y. Qin, Y. Wang, X. Sun, Y. Li, H. Xu, Y. Tan, Y. Li, T. Song, B. Sun, *Angew. Chem., Int. Ed.* 2020, **59**, 10619.

CAS | **PubMed** | **Web of Science®** | **Google Scholar**

Citing Literature

Download PDF

ABOUT WILEY ONLINE LIBRARY

Privacy Policy
Terms of Use
About Cookies
Manage Cookies
Accessibility
Wiley Research DE&I Statement and Publishing Policies
Developing World Access

HELP & SUPPORT

Contact Us
Training and Support
DMCA & Reporting Piracy

OPPORTUNITIES

Subscription Agents
Advertisers & Corporate Partners

CONNECT WITH WILEY

The Wiley Network
Wiley Press Room